Joule

CellPress

Article

Conjugated Organic Cations Enable Efficient Self-Healing $FASnI_3$ Solar Cells

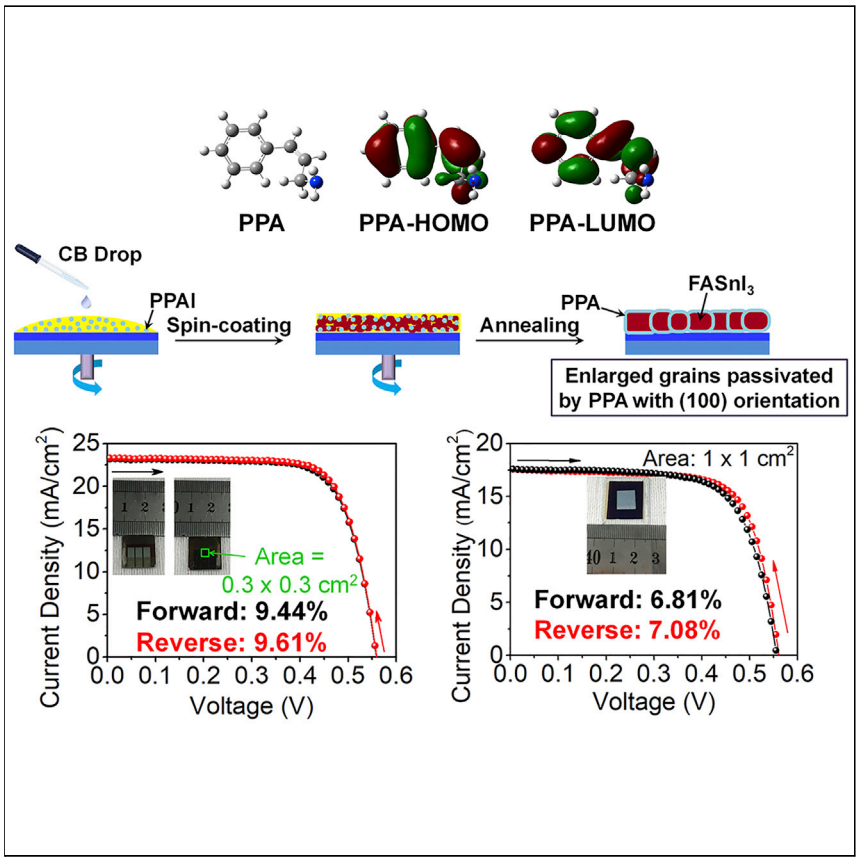

A conjugated large-volume cation is adopted as an additive to modify $FASnI_3$ film with much improved film quality. Lead-free PSC devices with PCE of 9.61% on 0.09 cm^2 and 7.08% on 1 cm^2 can be achieved. The PSC devices also show robust stability with self-healing ability. This work addresses the promise of Sn-based PSCs and takes a big step forward in the field of ecofriendly lead-free photovoltaic devices.

Chenxin Ran, Weiyin Gao, Jingrui Li, ..., Xun Hou, Mercouri G. Kanatzidis, Zhaoxin Wu

m-kanatzidis@northwestern.edu (M.G.K.)
zhaoxinwu@mail.xjtu.edu.cn (Z.W.)

HIGHLIGHTS

Conjugated cation is incorporated as an additive in tin perovskite for the first time

Film showing oriented grains with enlarged size and enhanced charge extraction

Solar cells with PCE of 9.61% on 0.09 cm^2 and 7.08% on 1 cm^2 are achieved

Robust device stability with self-healing behavior can be enabled

Ran et al., Joule 3, 3072–3087
December 18, 2019
https://doi.org/10.1016/j.joule.2019.08.023

Joule

CellPress

Article

Conjugated Organic Cations Enable Efficient Self-Healing $FASnI_3$ Solar Cells

Chenxin Ran,[1] Weiyin Gao,[1] Jingrui Li,[3] Jun Xi,[6] Lu Li,[1] Jinfei Dai,[1] Yingguo Yang,[2] Xingyu Gao,[2] Hua Dong,[1] Bo Jiao,[1,4,5] Ioannis Spanopoulos,[4] Christos D. Malliakas,[4] Xun Hou,[1] Mercouri G. Kanatzidis,[4,*] and Zhaoxin Wu[1,5,7,*]

SUMMARY

The introduction of large-volume amines (LVAs) in Sn-based perovskite films has been shown to lead to promising power conversion efficiency (PCE) in Pb-free perovskite solar cells (PSCs). However, the LVAs adopted so far (e.g., phenylethylammonium [PEA] and butylammonium [BA]) are insulating and could impede charge extraction within the perovskite film. Herein, a conjugated LVA, 3-phenyl-2-propen-1-amine (PPA), is introduced in formamidinium tin iodide ($FASnI_3$) perovskite. Our results show that the incorporation of PPA results in enlarged grain sizes, reduced trap density, preferential orientation, efficient charge extraction, and enhanced structural stability of $FASnI_3$ film. These positive effects help in achieving efficient PSCs with a PCE as high as 9.61% with negligible hysteresis and outstanding stability (remains 92% of its initial PCE value after 1,440 h). Furthermore, the presence of PPA enables a self-healing action of PSCs. Most importantly, we report large-area (1 × 1 cm^2) Sn-based PSCs achieving PCE of 7.08%.

INTRODUCTION

PSCs based on organic-inorganic lead (Pb) halide perovskite materials have made enormous progress because of their outstanding optoelectronic properties, defect tolerance, compositional flexibility, low-cost solution processing, and a power conversion efficiency (PCE) of ~24.2%.[1–6] The perceived toxicity problem of Pb in state-of-the-art PSCs, however, remains a concern that should be resolved on the path to commercialization.[7] With this in mind, researchers have made great efforts to develop PSCs based on Pb-free perovskite materials.[8–11] Among all Pb-free perovskite materials that show photovoltaic performance, formamidinium tin tri-iodide ($FASnI_3$)-based PSCs are the most promising because of the suitable band gap, low exciton-bind energy, and high carrier mobility.[12–34] The main drawbacks of Sn-based perovskite material are its instability, because of the easy oxidation of Sn^{2+} into Sn^{4+}, and high dark current, which arises from high *p*-type carrier concentration. The latter originates from the low formation energy of Sn vacancies.[35] Many strategies have been developed to overcome these problems and improve the performance of Sn-based PSCs. In one approach to avoiding the oxidation of Sn^{2+}, reduction additives (e.g., SnF_2,[29] pyrazine,[30] hydrazine vapor,[36] hydroxybenzene sulfonic acid or its salt,[37] and π-conjugated polymer[38]) and solvent-free processing[39] have been introduced and shown to be effective up to a point. In another type, Cs[33] or Br[34] alloying and construction of low-dimensional structures[13–20] in Sn-based perovskite have also been shown to be promising.

Context & Scale

For ecofriendly concerns, Sn-based PSCs have been extensively studied and made inspiring progress during the past few years. Recently, the introduction of large-volume amines (LVAs) (e.g., phenylethylammonium [PEA] and butylammonium [BA]) have shown their promise in enhancing the performance of $FASnI_3$-based PSCs. However, the insulating nature of these LVAs sets limitations on the charge extraction of the film. Herein, a conjugated LVA, 3-phenyl-2-propen-1-amine (PPA), is introduced aiming at promoting charge extraction within $FASnI_3$ film. The presence of PPA is found to enlarge the grain size, passivate the grains, and induce the orientation of the film. These merits of PPA deliver PSCs with PCE of 9.61% on 0.09 cm^2 and 7.08% on 1 cm^2. Moreover, PPA-based PSCs exhibit robust stability and self-healing behavior. This work sheds critical lights on improving the quality of perovskite film by molecular design of organic cations and highlights the promise of Pb-free PSCs.

Recently, low-dimensional structures have shown great potential in both Pb and Pb-free perovskite materials with the aim to improve their long-term stability.[40–43] LVAs such as phenylethylammonium (PEA)[16–19] and butylammonium (BA)[20] have been incorporated to stabilize the Sn perovskites with the formula $(LVA)_2FA_{n-1}Sn_nI_{3n+1}$ (where n is the number of SnI_6 octahedra between LVAs that defined the slab thickness). This quasi-2D structure defines a homologous family, which tends to have a lower dark carrier concentration than the 3D $FASnI_3$ and also features better stability, presumably by suppressing the oxidation of Sn^{2+} by confining the ion motions and diffusion from three dimensions to two.[43] However, because both the BA and PEA cations are insulating, we hypothesized that if we used a cation with a more conjugated and polarizable backbone, it may facilitate photoexcited charge transport both along and across the perovskite layers and in turn lead to improved solar-cell performance.

In this work, we introduce the use of a conjugated LVA, PPA, in solution to fabricate composite perovskite films. PPAI salt is adopted as an additive into $FASnI_3$ to partially replace FA, forming a precursor solution with the formula of $PPA_xFA_{1-x}SnI_3$. The presence of PPA is found to promote the formation of 3D perovskite grains with grain boundaries functionalized by PPA. In addition, the presence of PPA is shown to enlarge the grain size, induce preferential orientation, facilitate the charge extraction, and enhance the stability of $FASnI_3$ film. Because of these advantages, our inverted planar PSC based on PPA-modified $FASnI_3$ film shows a PCE of 9.61% with negligible hysteresis effects and robust device stability. Moreover, a self-healing effect is observed in the PPA-modified $FASnI_3$ film, which is assigned to the steric hindrance effect of PPA and the low formation energy of PPA-capped $FASnI_3$ structure. Most importantly, the first large-scale Sn-based PSC with active area of 1 cm^2 is reported, showing a PCE as high as 7.08%.

RESULTS AND DISCUSSION

Fabrication and Characterization of Perovskite Film

The synthesis procedure of PPA is following our previous work.[44] ^{1}H NMR spectroscopy (Figure S1) and Fourier transform infrared (FTIR) spectroscopy (Figure S2) were used to confirm the successful synthesis of PPA. Then, PPAI salt was synthesized following the typical synthesis process of MAI salt.[45] The ^{1}H NMR spectroscopy of PPAI confirms that the conjugated segment in PPAI is not destroyed after reacting with hydroiodic acid (Figure S3). It should be noted that for PPAI molecules, taking CH_3NH_3 group as a whole to occupy the A site in $FASnI_3$, the remaining part, C_6H_5-CH=CH-, is conjugated (Figure 1A). In order to prepare the $PPA_xFA_{1-x}SnI_3$ precursor solution with precise x values, precursor solutions of the nominal stoichiometry "$FASnI_3$" and "$PPASnI_3$" in dimethyl sulfoxide (DMSO) were separately prepared first. Then, $PPA_xFA_{1-x}SnI_3$ precursor solutions were prepared by mixing "$PPASnI_3$" and "$FASnI_3$" solutions with different x values (0%, 5%, 10%, 15%, 20%, and 40% in mole ratio) and stirred at room temperature to make a homogeneous solution. The antisolvent film-deposition protocol was used to fabricate the perovskite films.[46] Here, the perovskite films with different x values are labeled as 0% PPAI, 5% PPAI, 10% PPAI, 15% PPAI, 20% PPAI, and 40% PPAI, respectively. Because of the large volume of PPA molecule, PPA is not able to insert into the $FASnI_3$ lattice and could only replace the surface FA or passivate the FA vacancy at the surface of $FASnI_3$ structure (Figure 1B).

Figures 1C–1H show the SEM images of the prepared films with different PPAI contents, and it is evident that the grain size of the $FASnI_3$ film is enlarged when PPAI

[1]Key Laboratory for Physical Electronics and Devices of the Ministry of Education & Shaanxi Key Laboratory of Information Photonic Technique, School of Electronic and Information Engineering, Xi'an Jiaotong University, No.28, Xianning West Road, Xi'an 710049, China

[2]Shanghai Synchrotron Radiation Facility, Shanghai Institute of Applied Physics, Chinese Academy of Sciences, Shanghai 201204, P. R. China

[3]Department of Applied Physics, Aalto University, FI, 00076 AALTO, Finland

[4]Department of Chemistry, Northwestern University, 2145 Sheridan Road, Evanston, IL 60208, USA

[5]Collaborative Innovation Center of Extreme Optics, Shanxi University, Taiyuan 030006, China

[6]Global Frontier Center for Multiscale Energy Systems, Seoul National University, Seoul 08826, Korea

[7]Lead Contact

*Correspondence:
m-kanatzidis@northwestern.edu (M.G.K.),
zhaoxinwu@mail.xjtu.edu.cn (Z.W.)

https://doi.org/10.1016/j.joule.2019.08.023

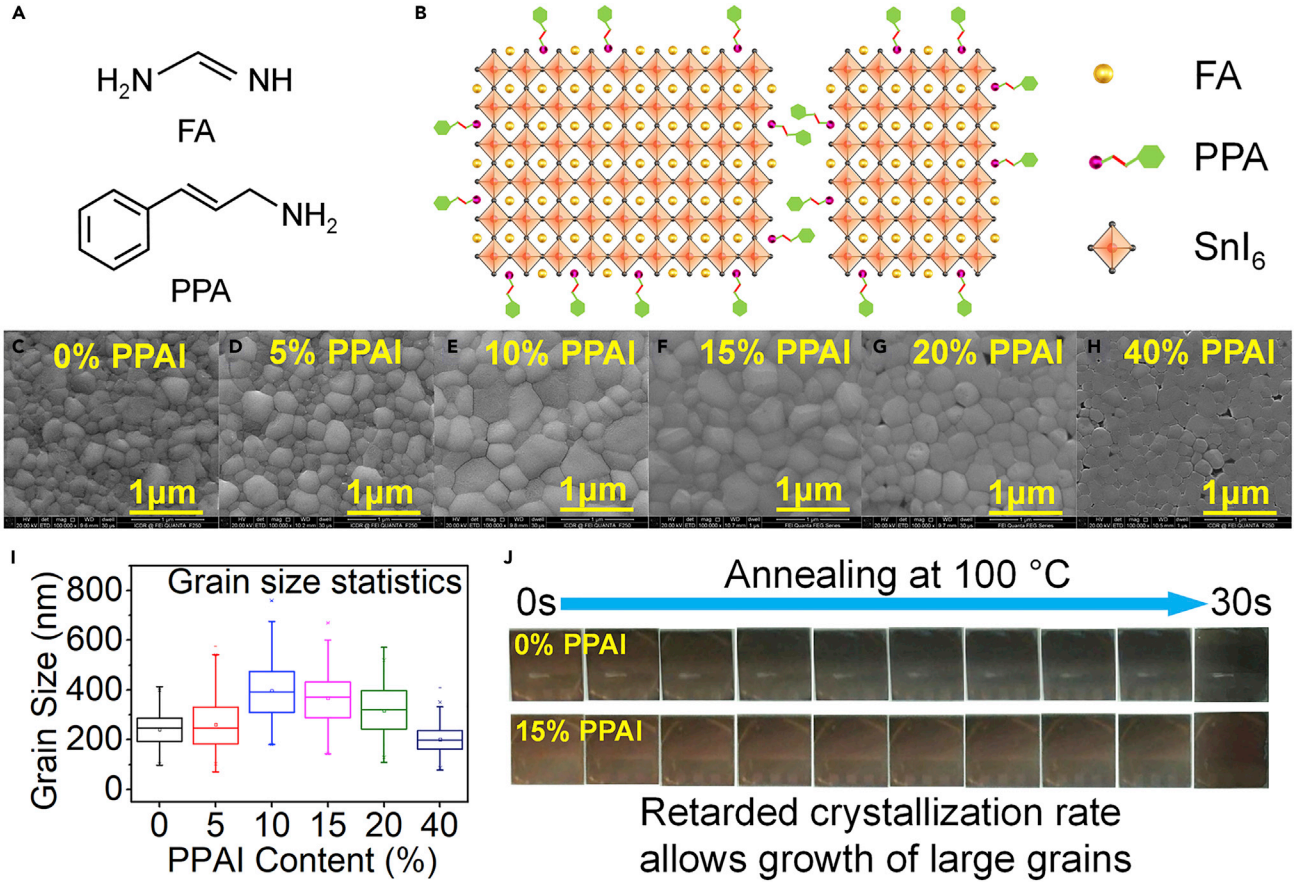

Figure 1. The Morphology of $PPA_xFA_{1-x}SnI_3$ Film

(A) Molecular formula of FA and PPA.

(B) Schematic representations of crystal structure of $PPA_xFA_{1-x}SnI_3$.

(C–H) SEM images of (C) 0% PPAI, (D) 5% PPAI, (E) 10% PPAI, (F) 15% PPAI, (G) 20% PPAI, and (H) 40% PPAI films. Scale bar: 1 μm.

(I) Statistics of grain-size distribution of $PPA_xFA_{1-x}SnI_3$ films with different PPAI contents, data are represented as mean ± SEM.

(J) Photographs of $FASnI_3$ films with and without PPAI during annealing at 100°C.

content increases from 0% to 10%. However, when the PPAI content exceeds 10%, the grain size begins to decrease (Figure 1I), which might originate from the high PPAI density that will confine the growth of large $FASnI_3$ grains. The growth mechanism of the $FASnI_3$ grains with and without PPAI can be explained by the Ostwald theory of ripening of crystals. In polycrystalline film, the size of the grains is determined by the crystallization rate of crystals, which is governed by the competition between nucleation rate and growth rate of crystals. The Ostwald ripening process normally involves two coupled steps: the first step is the dissolution of small-sized crystals because of their higher surface energy, whereas the second step is the growth of large-sized crystals with lower surface energy.[47] In other words, the Ostwald ripening process results from the suppression of the nucleation of crystals (corresponding to the first step) and facilitation of the growth of crystals (corresponding to the second step) the during film-forming process. The nucleation rate depends on the Gibbs energy barrier for crystal nucleation. If this energy barrier is low, the nucleation rate will be high, and small crystal will be rapidly formed before growing larger. This Gibbs energy barrier could be raised in the presence of suitable additives due to the chemical heterogeneity effect.[48] This raised barrier could retard the nucleation rate, which is slower than the growth rate, leading to the retarded

crystallization rate and facilitating the growth of large grains. Previous works have shown that a small amount of additive with large molecular volume could effectively enlarge the grain size in Pb-based perovskite film. For example, using urea,[49] NH_4SCN,[50] $NH_4H_2PO_2$,[51] N-rGO,[52] PCBM,[53] and polymers[54] as additives was found to passivate the grain boundaries (GBs) in perovskite film and enlarge the grain size, which is attributed to the Ostwald ripening growth of the grains. Therefore, for pure $FASnI_3$ film, the Gibbs energy barrier for nucleation could be low, and numerous nuclei and small grains are formed due to the high crystallization rate. By contrast, when a small amount of PPAI is presented, the Gibbs energy barrier for nucleation can be raised due to the chemical heterogeneity effect, which suppresses the nucleation while facilitates the growth of $FASnI_3$ crystal, resulting in the retarded crystallization rate and growth of large-sized grains. Figure 1J shows the photographs of $FASnI_3$ films with and without PPAI during annealing at 100°C, which demonstrates the retarded crystallization of the film when PPAI is presented.

To investigate the influence of PPA on the orientation of the films, two-dimensional grazing incidence X-ray diffraction (2D-GIXRD) was carried out. The pure $FASnI_3$ film (0% PPAI) shows typical diffraction ring at $q \approx 1.0$, 1.7, 1.9, and 2.2 $Å^{-1}$, corresponding to (100), (120), (200), and (122) crystal planes of $FASnI_3$ (Figure 2A), which demonstrates its random orientation.[15] After the incorporation of 15% PPAI (Figure 2B), however, the intensity of the diffraction rings of (100) and (200) planes increased while that of (122) plane decreased. The radially integrated intensity plots along the (100) ring at $q \approx 1$ $Å^{-1}$, plotted as a function of azimuthian angle are depicted in Figure 2C. The emerging peak at the azimuthian angle of 90° demonstrates the preferential in-plane (100) orientation of $FASnI_3$ after PPAI addition.[55,56] Besides, no Bragg spots of 2D perovskite are presented in the 15% PPAI film. Moreover, the root-mean-square (RMS) roughness of the film decreases from 13.14 nm (0% PPAI) to 7.09 nm (40% PPAI) (Figure S4), also implying preferential orientation along (*h*00) planes parallel to the substrate.

The crystal structure of PPA-modified $FASnI_3$ films were further characterized by X-ray diffraction (XRD) as shown in Figure 2D. The XRD patterns of all the films are calibrated by the diffraction peak of ITO at ~ 30.5° as standard (Figure S5). The pure $FASnI_3$ film shows diffraction peaks at angles of 14°, 24°, 28°, 32°, and 41° that belong to the diffraction planes of (100), (120), (200), (122), and (222) of the orthorhombic (*Amm*2) space group, respectively (Figure S6). In contrast, the $FASnI_3$ films modified by increasing content of PPAI exhibit enhanced intensity of (100), (200), and (300) peaks while suppressed intensity of (120), (122), and (222) peaks. Besides, no diffraction peaks of 2D perovskite are observed in PPA-modified films. These results are consistent with the 2D-GIXRD result. The overall structural refinement of the XRD patterns was carried out using Jade software, and the refined parameters obtained from the analysis are listed in Table S1. It can be seen that all of the crystal structures of PPA-modified $FASnI_3$ films match to the orthorhombic phase in the space group of *Amm*2. This result indicates that PPA molecules locate at the crystal surface instead of inserting into the crystal lattice of $FASnI_3$. What's more, the presence of PPA is shown to alter the bond length along the *a* axis and leads to a shrunken cell volume, which, in turn, agrees with the optimized crystal structure of PPA-capped $FASnI_3$ obtained from density-functional-theory (DFT) calculations showing a distorted SnI_6 octahedral framework (Figure S7C). Furthermore, the crystal size evolution estimated from FWHM of (100) peak agrees well with the grain-size evolution obtained in SEM images (Figure 1I). To sum up, the growth of $FASnI_3$ grains with and without PPAI can be depicted as follows: Without PPAI, the rapidly formed $FASnI_3$ seeds after antisolvent dropping will spontaneously grow

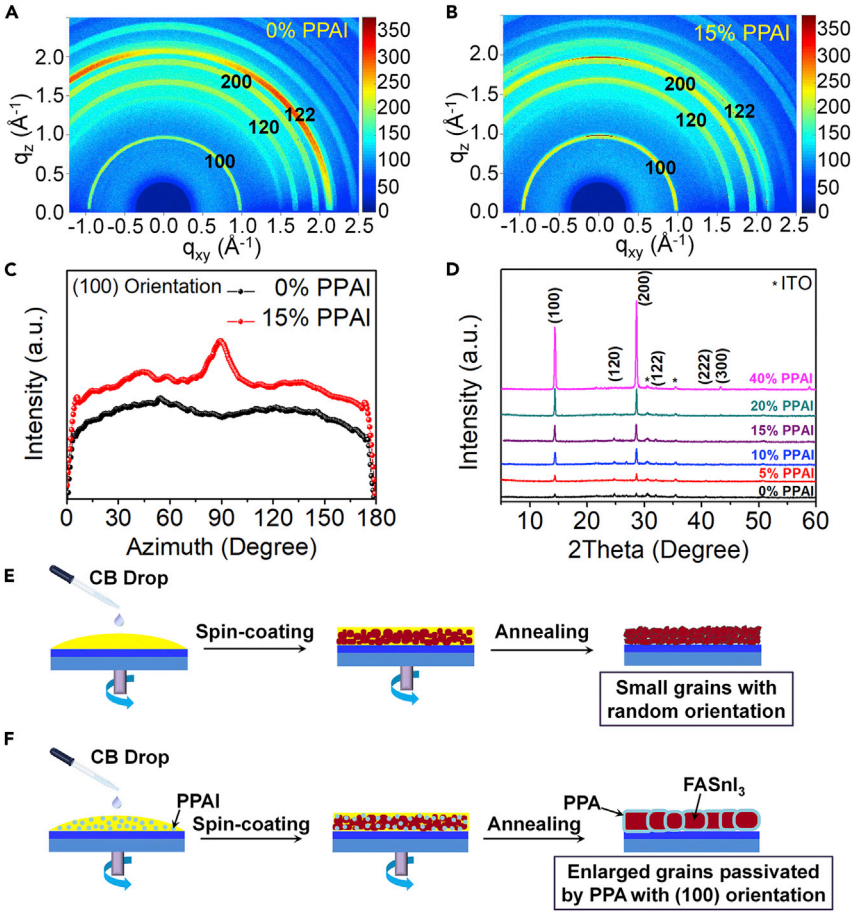

Figure 2. The Structure of PPA-Passivated $FASnI_3$

(A and B) 2D-GIXRD profiles of PPAI films (A) 0% PPAI, (B) 15% PPAI.

(C) Radially integrated intensity plots of the GIXRD profiles along the ring at $q \approx 1$ Å^{-1} corresponding to the (100) orientation of the $FASnI_3$ structure.

(D–F) XRD patterns of $PPA_xFA_{1-x}SnI_3$ films with different PPAI contents (D). Schematic diagram of the film forming process of the $FASnI_3$ film (E) without or (F) with PPAI introduction.

into small grains with random orientation after the post-annealing process (Figure 2E). However, when PPA is presented, PPA could suppress the nucleation and promote the growth of crystal seeds into larger gains due to the Ostwald ripening, and PPA will locate at the boundaries of the enlarged $FASnI_3$ grains and induce the preferential orientation (Figure 2F).

It is worth noting that because $PPA_xFA_{1-x}SnI_3$ is different from quasi-2D structure of $PPA_2FA_{n-1}Sn_nI_{3n+1}$ (insufficient PPA in $PPA_xFA_{1-x}SnI_3$), an excess of SnI_2 will be created. Excess metal halides in perovskite have been reported to have impact on grain size, morphology, and orientation.[57] To exclude the influence of excess SnI_2, we fabricated $FASnI_3$ film with 10% SnI_2 excess for comparison. SEM, grain size distribution, and XRD results can be found in Figure S8. It can be seen that although the grain size slightly enlarges, distinguished pinholes appear between grains. In addition, unlike 10% PPAI film showing significant enhanced (*h*00) peak intensity, $FASnI_3$ film with 10% SnI_2 excess still shows weak peak intensity similar to $FASnI_3$ film. These results demonstrate that only addition of excess SnI_2 has limited influences on grain size, morphology, and orientation of $FASnI_3$ film, underlying the key role of PPA in

determining the features of $FASnI_3$ film. Last but not the least, we found that even when no FA is involved (i.e., $x = 1$), $PPASnI_3$ film also shows no typical features (morphology, crystal structure, and optical property) of 2D structure (PPA_2SnI_4), as shown in Figure S9. This indicates that a precursor with formula of $PPA_xFA_{1-x}SnI_3$ cannot form typical quasi-2D structures with formula of $PPA_2FA_{n-1}Sn_nI_{3n+1}$. These differences between $PPASnI_3$ and PPA_2SnI_4 are interesting, but beyond the scope of this work. This could inspire more work related to this issue in the future.

The optical properties of PPA-modified $FASnI_3$ films were further characterized by UV-Vis absorbance and photoluminescence (PL) spectroscopy (Figure S10). The slight blue shifting of the absorption edge as well as PL peak position (862 to 856 nm with increasing PPAI content) can be observed, indicating a slightly enlarged band gap (from 1.43 eV to 1.45 eV) (Figure S10C). This enlarged band gap could be beneficial in improving the open circuit voltage (V_{OC}) of PSCs. Besides, no other PL peaks are observed in the range from 500 to 750 nm (Figure S10B), which also suggests the absence of the low-dimensional perovskite. We then investigated the origin of the blue shift of PPA modified $FASnI_3$ using DFT calculations. The band structures of $FASnI_3$ with and without PPA capping are qualitative investigated (Figure S7). When $FASnI_3$ is capped by PPA molecules, an enlarged band gap can be obtained compared with pure $FASnI_3$, which is in agreement with the observed blue-shifted PL. The optimized geometry relaxation of $FASnI_3$ and PPA-capped $FASnI_3$ indicates that the presence of PPA on $FASnI_3$ leads to a distorted SnI_6 octahedral framework (Figure S7C), which is also revealed by XRD refinement results (Table S1). Thus, this structure variation could be the origin of the enlarged band gap as well as blue-shifted PL of PPA-capped $FASnI_3$.

In addition to inducing morphology improvement and crystalline orientation, the presence of PPA is also found to enhance the stability of $FASnI_3$ film. An *in situ* UV−Vis evolution experiment was carried out to monitor the change of absorbance spectra of perovskite films exposed to the ambient environment (Figure S11A and S11B). For $FASnI_3$ film, an obvious decrease of absorbance over the whole spectrum region was observed during a time period of 60 min. By contrast, the absorbance spectra of 15% PPAI film show negligible change over a time period of 60 min. This result clearly demonstrates the improved air stability of PPA-modified film. To investigate the origin of the improved stability, we compared the Sn^{4+} content in the $FASnI_3$ film with and without PPAI using X-ray photoelectron spectroscopy (XPS) (Figure S11C). It is observed that the Sn^{4+} proportion in PPAI film is much lower than that in pure $FASnI_3$ film, implying that the presence of PPA prevents Sn^{2+} from oxidizing during the film-forming process. It is found that PEAI film shows a slightly higher Sn^{4+} content than PPAI film (Figure S12), which might be due to the 2D-3D structure formed in PEAI film.[16] It is a general consensus that the instability of Sn-based perovskite is due to the easy oxidation of Sn^{2+} and the presence of Sn^{4+} in the film.[18] Therefore, the lower proportion of Sn^{4+} in PPA based film leads to the enhanced stability of the film, which could be beneficial to the stability improvement of PSC devices.

Fabrication and Photovoltaic Performance of PSCs

The photovoltaic performance of PPA-modified $FASnI_3$ film was measured by fabricating inverted planar heterojunction PSCs based on the configuration of ITO/PEDOT: PSS/perovskite/C_{60}/BCP/Ag. See Figure 3A for a cross-sectional SEM image of a typical device. The effect of PPA on the performance of PSCs is carefully studied by optimizing the PPA content and precursor concentration (Figures 3B and S13). Table S2 collects all the performance parameters of these PSCs. The

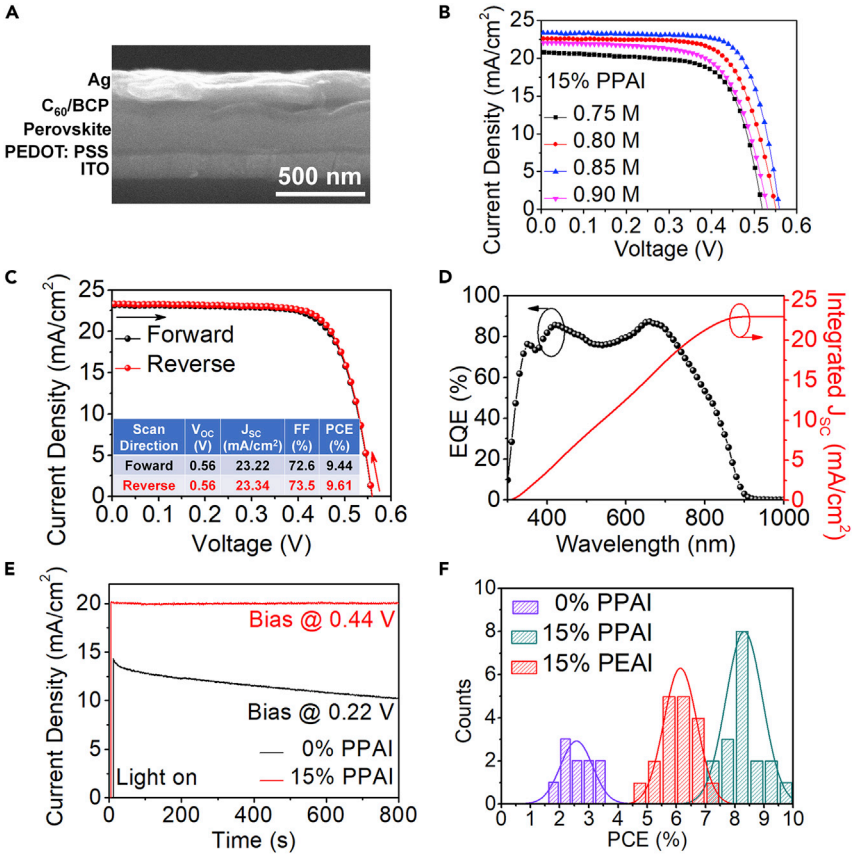

Figure 3. The Performance of PPA-Passivated $FASnI_3$ Solar Cell

(A) Cross-sectional SEM image of PSCs with inverted device structure, the scale bar is 500 nm.

(B) Current-voltage (*J-V*) curves of 15% PPAI device under different precursor concentrations.

(C) *J-V* curves of the best-performing PSC device with different scanning directions; inset shows the photograph of PSC device.

(D) The EQE spectra and integrated J_{SC} of the best-performing PSC device.

(E) The stabilized photocurrent densities of the PSCs with or without PPAI addition for 800 s.

(F) Histograms of 18 PSCs from three batches using three different additives fabricated under the same experimental conditions.

incorporation of PPA clearly improves all the photovoltaic parameters (V_{OC}, J_{SC}, FF, and PCE) with respect to the control device without any PPA, and this is in agreement with the improved quality of $FASnI_3$ films after when PPA is presented as characterized above. The 15% PPAI PSCs show the highest PCE with a V_{OC} of 0.56 V, J_{SC} of 23.22 mA/cm^2, FF of 72.6%, and PCE of 9.44% by forward scan, and a V_{OC} of 0.56 V, J_{SC} of 23.34 mA/cm^2, FF of 73.5%, and PCE of 9.61% by reverse scan (Figure 3C). The PCE of 9.61% is among the highest reported PCE for Sn-based PSC devices so far (Table S3). Further increase in the PPAI content, however, leads to decreased performance, which may result from the lowered fraction of $FASnI_3$ in the active absorber when the PPAI content is high. The external quantum efficiency (EQE) spectrum of 15% PPAI film (Figure 3D) shows broad light response ranging from 300 nm to 900 nm, which is consistent with the absorption spectrum of the film. In addition, the integrated J_{SC} calculated from the EQE spectrum is 22.96 mA/cm^2, which agrees well with the measured J_{SC} from *J-V* curve. The bandgap of $FASnI_3$ films with and without PPA are estimated by measuring UV photoelectron spectroscopy (UPS) of the films (Figures S14A–S14D). The valence band maximum (VBM) is found to deepen from -4.93 eV to -5.19 eV upon the PPAI introduction. Based on the

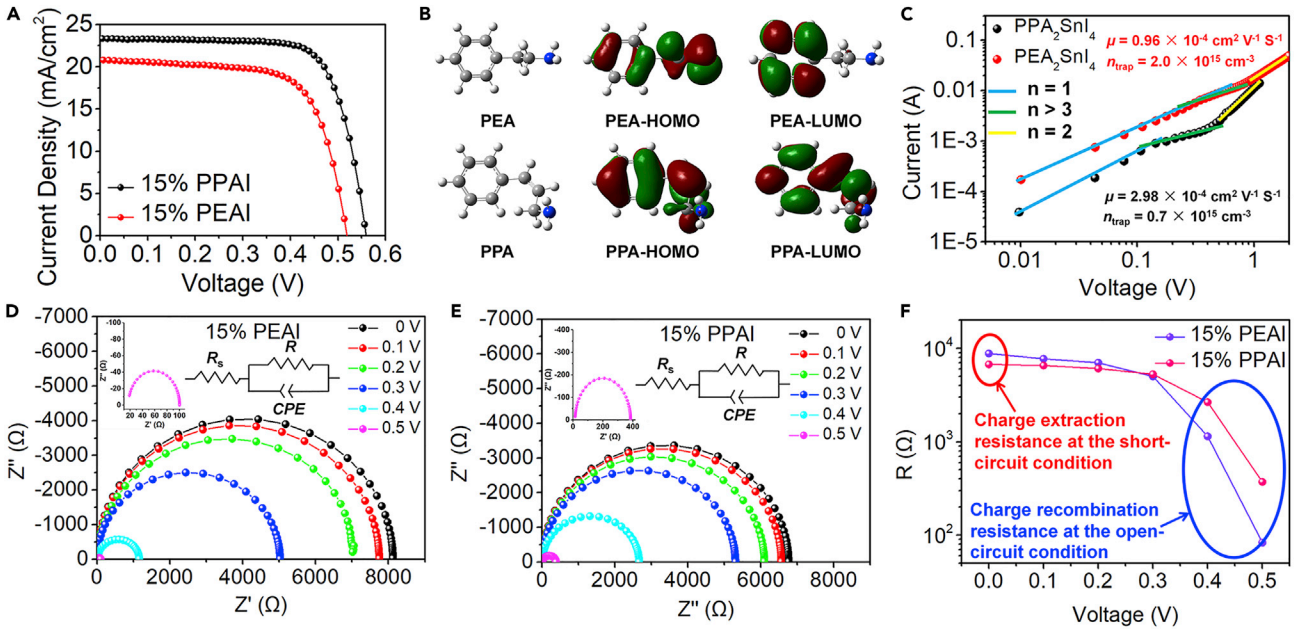

Figure 4. Charge Transport, Extraction, and Recombination Behaviors in PPA-Passivated $FASnI_3$ Solar Cells

(A) *J-V* curves of best-performing PSCs based on 15% PPAI and 15% PEAI.

(B) Optimized geometrical structures, HOMO, and LUMO distributions of PEA and PPA molecule by DFT calculations at B3LYP and 6–31G (d) levels.

(C) SCLC measurements of PPA_2SnI_4 and PEA_2SnI_4 films.

(D and E) Nyquist plots of the EIS measurement of (D) 15% PEAI and (E) 15% PPAI at different applied biases under 1 sun illumination. Inset in (D) and (E) shows the equivalent circuit model used for the fitting of EIS results, where R_S is the sheet resistance, and R is related to the resistance of perovskite layer.

(F) The fitted R at different applied biases obtained from the EIS analysis.

bandgap of the films calculated from the Tauc plot (Figure S14E), the conduction band minimum (CBM) is estimated to be around -3.54 eV and -3.77 eV for 0% PPAI and 15% PPAI, respectively. From the diagram of energy-level alignment of PSCs (Figure S14F), it can be observed that compared with pure $FASnI_3$ film, the deepened VBM and CBM of 15% PPAI film enables a better energy-level matching to the PEDOT: PPS layer and C_{60} layer, respectively. This more favorable energy alignment could promote the charge transfer at the both interfaces, contributing to the enhanced photovoltaic performance of PPAI PSC devices.

The stabilized photocurrent at the maximum output powers of the devices with or without PPA are shown in Figure 3E; it can be seen that the 0% PPAI devices show a gradual decrease in photocurrent density, while 15% PPAI device is stabilized with a steady-state photocurrent of ~ 20 mA/cm^2 at 0.45 V bias under constant light irradiation for more than 800 s. Systematic stability tests of devices will be presented later. In addition to the enhanced PSCs performance and device stability, the device reproducibility is also improved when PPA is presented (Figure 3F). Here, we also fabricated PSCs using 15% PEAI as an additive for comparison purposes. It can be seen that 15% PPAI devices exhibit superior photovoltaic performance parameters over the control (0% PPAI) and 15% PEAI devices (Figure S15).

Efficient Charge Extraction of PPA-Modified $FASnI_3$

It is found that using PPAI as an additive in our work, a higher device performance can be obtained over that using PEAI (Figure 4A). Conjugated segments in PPA molecules might be the origin of the superior device performance compared to PEA.

Molecular electronic structure calculations were carried out to show the electronic distribution on PPA and PEA molecules (Figure 4B). The calculations suggest that the electron density in LUMO of PPA delocalizes widely in the conjugated part, suggesting the superior electron-transport ability on PPA molecule. Space-charge-limited-current (SCLC) measurements were further adopted to study the role of the conjugated segment in PPA (Figure 4C). Here, to focus on the conductivity of organic molecule and exclude other factors that could impact the conductivity of the films, PPA_2SnI_4 and PEA_2SnI_4 films were deposited for measurement. By fitting the Child's regime (n = 2) at high voltage (Supplemental Information for detailed calculations method), it is found that the charge mobility of PPA_2SnI_4 film is three times higher than PEA_2SnI_4 film (2.98×10^{-4} cm^2 V^{-1} s^{-1} versus 0.96×10^{-4} cm^2 V^{-1} s^{-1}), suggesting the better charge transport of the conjugated PPA molecule. In addition, SCLC measurements of 0% PPAI and 15% PPAI films (Figure S16) show that after the introduction of 15% PPAI, the trap density decreased from 5.05×10^{15} cm^{-3} to 3.47×10^{15} cm^{-3}, while the mobility increased from 3.80×10^{-4} cm^2 V^{-1} s^{-1} to 4.14×10^{-4} cm^2 V^{-1} s^{-1}. This result demonstrates that PPA could passivate the defect trap state and improve the charge transport within the $FASnI_3$ film.

Electrochemical impedance spectroscopy (EIS) was further carried out to study the electronic properties of 15% PPAI- and 15% PEAI-based PSCs devices. The measurement was tested under 1 sun illumination with different applied biases. By fitting the EIS spectra at different applied biases from 0 V – 0.5 V (Figures 4D and 4E), the evolution of resistance can be obtained (Figure 4F). According to the previous literature,[58,59] at the short-circuit condition (i.e., bias at 0 V), the resistance (R) is dominated by charge transport of the perovskite film, while at open-circuit conditions (i.e., bias at V_{OC}), R is dominated by charge recombination at the interfaces of the film. As shown in Figure 4F, at applied bias of 0 V, the PPA device shows a lower R than the PEAI device, indicating the efficient charge transport within PPA film, which is in agreement with the more delocalized electron distribution and higher charge mobility of PPA molecule as shown in Figures 4A and 4C, respectively. However, a higher R of PPA devices is observed when the applied bias is higher than 0.3 V. In this bias range approaching V_{OC} (0.3 V – 0.5 V), R will be dominated by the charge recombination resistance at the interfaces of the film. Therefore, the higher R of the PPA device indicates the lower charge recombination rate and more efficient charge extraction compared with the PEA device. This result also agrees with the lower V_{OC} and FF of the PEA device as shown in Figure 4A. In addition, only slight drop of J_{SC} is observed in both PPA- and PEA-based devices after EIS measurement (Figure S17), demonstrating the robust stability of both films. We further tested the stabilized photocurrent densities at maximum power output under 1 sun illumination for both PPA and PEA devices for a period of 10,000s (Figure S18). Almost no degradation is observed after continuous illumination for 10,000s, indicating the superior working stability of both devices. These results suggest that the structure of PPA-capped $FASnI_3$ film is also stable compared with the 2D/3D structure of PEA-based $FASnI_3$ film.[16] In addition, compared to 0% PPAI device, 15% PPAI device shows much improved charge recombination resistance at V_{OC} bias under 1 sun illumination (Figure S19), suggesting an efficient charge extraction when PPA is presented.

Improved Stability and Self-Healing Performance

The stability of PPA-modified devices was carefully studied. All tests are based on unencapsulated devices. Figure 5A shows the stability of PSCs stored in N_2. The efficiency of the 0% PPAI device decays to 12% of its original PCE, while the 15% PPAI device retains 92% of its initial PCE value after 1,440 h (60 days) (stored in glovebox

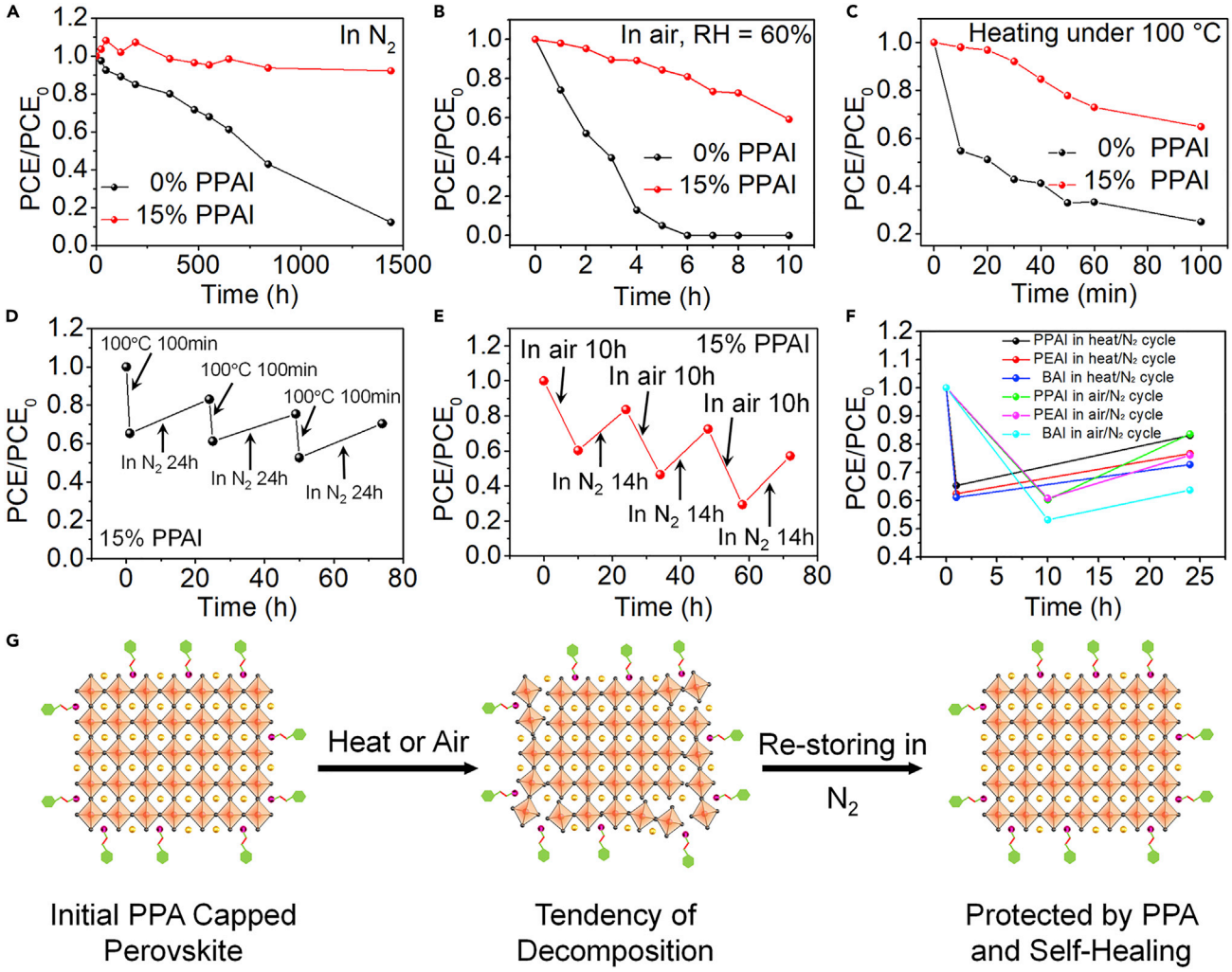

Figure 5. The Stability of PPA-Passivated $FASnI_3$ Solar Cell and Its Self-Healing Effect

(A–E) Normalized PCE of $FASnI_3$ PSCs with or without PPAI addition under the conditions of (A) storing in N_2., (B) in air, and (C) heating at 100°C. The self-healing effect of 15% PPAI device during (D) heating-N_2 cycles, and (E) air-N_2 cycles.

(F) PCE variations of BA-, PEA-, PPA-based devices during different testing cycles.

(G) Possible mechanism of the self-healing effect in PPA capped $FASnI_3$ structure.

without illumination except for *J-V* measurement at intervals). The degradation of the 0% PPAI device may be due to its inferior structural stability because of the high defect density in $FASnI_3$ film and trace of H_2O and O_2 presented in the glove box. By contrast, the introduction of PPA could enhance the structural stability by passivating the defects trap state and repelling moisture because of its hydrophobic nature. The protection of $FASnI_3$ from H_2O and O_2 is further evidenced by the stability test of PSCs stored in air as shown in Figure 5B. At 60% room humidity in air, the PSC device with 15% PPAI still retains ~ 60% of its initial PCE value after 10 h, while the 0% PPAI device is rapidly disabled after 6 h. In addition, the thermal stability of the 15% PPAI device is also shown to be enhanced (Figure 5C). The 15% PPAI device retained ~ 60% of its initial PCE value after continuous heating at 100°C for 100 min, while the 0% PPAI device losses ~ 80% of its PCE value. From the above characterizations, it has been proved that using PPAI as an additive introduces the passivation, orientation, and effective charge transport and extraction of $FASnI_3$ film. And all

these advantages should synergistically contribute to the improved efficiency and stability of the PSCs devices.

Interestingly, we observed an interesting self-healing effect in PPA-based devices. After heating (Figure 5D) or exposing to air (Figure 5E), the PPA device was able to partially restore its photovoltaic performance after being placed in N_2 atmosphere for a given time period. For example, after heating at 100°C for 100 min, the PCE of 15% PPAI device dropped to ~ 60% of its initial value. After it was placed in N_2 for 24 h, the device regained up to ~ 80% of its initial PCE value, and this self-healing effect could be repeated during the three heating-N_2 cycles (Figure 5D). A similar effect was also observed in performing air-N_2 cycles (Figures 5E, S20A, and S20B). By contrast, the 0% PPAI device showed no such effects (Figures S20C and S20D). Considering the different molecule volumes of LVAs, the self-healing effect is proposed to be attributed to the steric hindrance effect of the LVAs. And a molecule with larger volume should have a stronger steric hindrance effect. To verify this, we further used two other LVAs (i.e., PEA and BA) as additives for comparison (Figure 5F). Interestingly, BA and PEA devices also show self-healing effect both in heat-N_2 and air-N_2 cycles. However, the self-healing ability of the three LVCs is different. Table S4 and Table S5 show the PCE variation and self-healing rate of PSCs devices based on different LVAs during air-N_2 and heating-N_2 cycles, respectively. It can be seen that the self-healing ability of LVAs follows the order of PPA>PEA>BA, which follows the same order of the molecule volume of PPA>PEA>BA as shown in Figure S21. This result confirms that the self-healing effect should be attributed to the steric hindrance of the LVAs, and devices based on LVAs with larger volume show stronger self-healing ability.

To further understand the superior stability and self-healing of PPA-based PSCs, we carried out first-principles DFT calculations to investigate the structural stability of $FASnI_3$ capped by different LVA molecules (LVA = BA, PEA, PPA) (Figure S22). The calculation results demonstrate that the formation energy of the structures follows the order of PPA<PEA<BA, that is, PPA-capped structure shows the highest structural stability among the three structures. The low formation energy could make it easier for the $FASnI_3$ structure to reconstruct after restoring in N_2. Therefore, in addition to PPA's steric hindrance effect, the robust stability and durability of PPA-based PSCs could also be derived from the prominent thermodynamic stability of PPA-capped $FASnI_3$ structure.

Based on the experimental and theoretical studies above, the self-healing process might be depicted as shown in Figure 5G, where we used the PPA-capped $FASnI_3$ as an example. After heating or storing in air, the sensitive $FASnI_3$ structure has a tendency to decompose. However, the presence of PPA molecules on $FASnI_3$ surfaces imposes restrictions on the decomposed fragments (i.e., FA, SnI_6) from falling or moving apart. Thus, after restoring in N_2, due to the low formation energy of PPA capped $FASnI_3$, the $FASnI_3$ structure is possible to reconstruct. In other words, even after partial degradation, the protective PPA capping layers may still hold up all the disassembled building blocks into the same confined space. And in this scenario, the $FASnI_3$ structure is able to reassemble when the device is placed in an inert atmosphere.

Large-Scale Sn-based PSCs

The photovoltaic performance of large-scale devices is important for the commercialization of Pb-free PSCs.[60] We therefore fabricated large-scale PSCs based on the PPA-modified $FASnI_3$ film. A 15% PPAI device with active area of 1 cm^2 was fabricated (Figures 6A and 6B), which is the first example of large-scale Sn-based PSCs

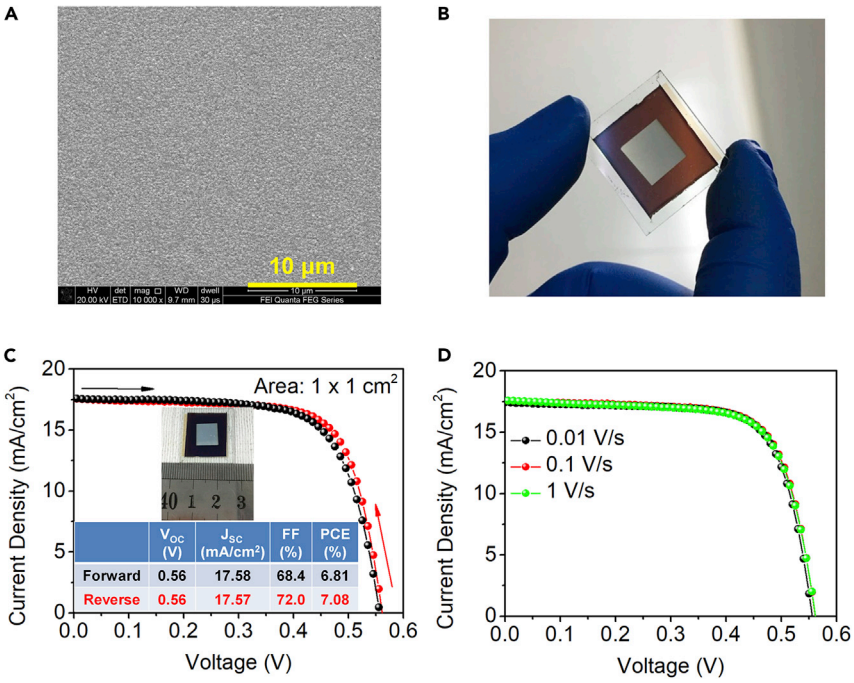

Figure 6. PPA-Passivated $FASnI_3$ Solar Cells with Active Area of 1 × 1 cm^2

(A and B) SEM (A) and (B) photograph images of 15% PPAI PSCs, the scale bar in SEM image is 10 µm.

(C) *J-V* curves of the best-performing large-scale PSC device with different scanning directions and inset shows the photograph of the device with an active area of 1 cm^2.

(D) *J-V* curves of the large-scale PSC device with different scan rates.

reported so far. The best-performing device shows a V_{OC} of 0.56 V, J_{SC} of 17.58 mA/cm^2, FF of 68.4%, and PCE of 6.81% by forward scan, and a V_{OC} of 0.56 V, J_{SC} of 17.57 mA/cm^2, FF of 72.0%, and PCE of 7.08% by reverse scan (Figure 6C). The device also shows no change in photovoltaic performance under different scan rates (Figure 6D). In addition, the device shows high uniformity in photovoltaic performance when covered by shadow masks with 0.075 and 0.046 cm^2 active areas at different positions (Figure S23).

When measuring the *J-V* curve of the large-scale device covered by shadow masks with different active areas, we observed a decreased V_{OC} and FF when the area of shadow mask decreased from 1 cm^2 to 0.046 cm^2 (Figure S24). This could be due to the higher series resistance as the collected holes transfer on large-area ITO when shadow masks are applied. To identify this effect, we further tested the *J-V* curves of small-area PSCs covered by different shadow masks (Figure S25). A similar tendency (decreased V_{OC} and FF) can be observed in small-area PSCs when the area of shadow mask decreased from 0.09 cm^2 to 0.046 cm^2. However, the losses of V_{OC} and FF are much smaller than that in the large-area device. This is because the collected holes on the small-area device transfer through a shorter distance than that on large-area device when shadow masks are applied, and the series resistance is smaller when transport occurs over a shorter distance.

Conclusion

In conclusion, a conjugated LVA, PPA, is introduced in $FASnI_3$ perovskite precursor solutions to prepare films with improved photovoltaic performance. There are three

main benefits of introducing PPA in $FASnI_3$: (1) improved film quality (enlarged grain size, preferential orientation, and lowered trap density); (2) enhanced charge transport and extraction; and (3) superior stability and self-healing effect of PSC devices. The inverted PSCs fabricated based on PPA-modified $FASnI_3$ film exhibit a PCE of 9.61%, which is among the highest value reported so far for Sn-based PSCs. Most importantly, we demonstrated large-scale (1 cm^2) Sn-based PSCs with a promising PCE of 7.08%. This work provides a valid approach to balance the stability and charge extraction in Sn-based perovskites and highlights the great potential for boosting efficiencies in Sn-based PSCs.

EXPERIMENTAL PROCEDURES

Materials

PEDOT: PSS (Clevios Al4083, Haraeus), SnI_2 (99.99%, Sigma Aldrich), SnF_2 (99.5%, Sigma Aldrich), FAI (99%, MaterWin New Material), BCP (99%, Nichem), chlorobenzene (anhydrous 99.8%, Sigma Aldrich), and DMSO (anhydrous 99.8%, Alfa Aesar) were used as received. PPA is synthesized following our previous work.[44] PPAI salt is prepared following the same process of typical MAI salt.[45]

Film Deposition

To prepare PPA-modified $FASnI_3$ film, $FASnI_3$ and $PPASnI_3$ precursor solutions were first prepared by dissolving 316.6 mg SnI_2 (0.85 mmol), 146.2 mg FAI (0.85 mmol), and 13.3 mg SnF_2 (0.085 mmol) respectively, in 1 ml DMSO and stirred for 2 h under room temperature to form a 0.85 M solution. Then different mole ratios of the $FASnI_3$ and $PPASnI_3$ solutions (0%, 5%, 10%, 20%, 40%) were mixed to prepare the PPA, FAI, and SnI_2 precursor solutions. To fabricate PPA-modified $FASnI_3$ films, the precursor solution was spin-coated on the substrate at 5,000 rpm for 60 s, and 100 μL chlorobenzene was dropped at the 30th sec after spinning started. Finally, the film was dried at 40°C for 2 min and 100°C for 20 min.

Film Characterization

Field emission scanning-electron microscope (SEM) (Quanta250, FEI, USA) and atomic force microscope (AFM, NT-MDT, Russia) were used to investigate the morphology of perovskite film. XRD measurements were performed with an X-ray diffractometer (D/MAX-2400, Rigaku, Japan) with Cu Kα radiation. The absorption spectra were acquired on a UV-Vis spectrophotometer (U-3010, Hitachi High-Technologies, Japan). The PL spectra were acquired on a photoluminescence spectroscopy (Fluoromax 4, HORIBA Jobin Yvon, United States). FTIR spectra were measured with a PerkinElmer FT-IR spectrometer. EIS experiments were carried out in under AM 1.5 illumination at 0 V with an electrochemical workstation (CHI660C, CH Instruments) in a frequency range from 0.1 Hz to 1 mHz. The GIXRD measurements were performed at the BL14B1 beamline of Shanghai Synchrotron Radiation Facility (SSRF) using X-rays with a wavelength of 0.6887 Å, and the incident angle set to 0.3°. The 2D-GIXRD patterns were analyzed using Fit 2D software and displayed in scattering-vector q coordinates with $q = 4\pi \sin \theta/\lambda$, where θ is half of the diffraction angle, and λ is the wavelength of the incident X-ray. EIS experiments were carried out in under AM 1.5 illumination at different applied biases with an electrochemical workstation (CHI660C, CH Instruments) in a frequency range from 0.1 Hz to 1 mHz. The UPS measurements were carried out by X-ray photoelectron spectroscopy using Au as reference (ESCALAB Xi+, Thermo Fisher Scientific).

Device Fabrication

The ITO substrate was sequentially cleaned with ultrapure water, acetone, ethanol, and isopropanol. After 10 min of UV-O_3 treatments, the PEDOT: PSS solution was filtered and spin-coated onto the substrate at 5,000 rpm for 60 s and then annealed 20 min at 170°C. After the deposition of the perovskite layer, C_{60} (30 nm) and BCP (8 nm) were sequentially evaporated at the rate of 1.0 Å/s. Ag (120 nm) was finally evaporated through a shadow mask with an active area of 0.09 cm^2 or 1 cm^2 to finish the small-area and large-area devices, respectively. After fabrication, all devices were kept unencapsulated in the glovebox for further measurements.

Device Characterization

All measurements were conducted in ambient air. The photovoltaic performance was measured under an AAA solar simulator (XES-301S, SAN-EI), AM 1.5G irradiation with an intensity of 100 mW/cm^2 with shadow masks. The photocurrent-voltage (J-V) curve was measured using a Keithley 2602 Source-Meter. Incident photon-to-current conversion efficiency (IPCE) spectra were collected by the solar-cell quantum-efficiency measurement system (SolarCellScan 100, Zolix instruments. Co. Ltd.).

For SCLC measurement, the device structure of ITO/PEDOT: PSS/perovskite/Au was used. The trap-state density in the film can be estimated by the equation:[3]

$$n_{\mathrm{trap}} = 2\epsilon_0\epsilon V_{TFL}/qL^2$$

where ϵ is the vacuum permittivity, ϵ_0 is the static dielectric constant of $FASnI_3$ (~5.7), q is the elemental charge, and L is the thickness of the film. The charge mobility in the film can be estimated by the Mott-Gurney equation:[3]

$$\mu = 8JL^3/9\epsilon_0\epsilon V^2$$

where J/V^2 is the slope of J versus V^2 (n = 2) in Child's regime (yellow curves) in Figure 4C.

SUPPLEMENTAL INFORMATION

Supplemental Information can be found online at https://doi.org/10.1016/j.joule.2019.08.023.

ACKNOWLEDGMENTS

This work was financially supported by the National Natural Science Foundation of China (grant nos. 61935016, 11574248, 51802253), the Fundamental Research Funds for the Central Universities (grant nos. xjj2018018 and xjj2016031), and China Postdoctoral Science Foundation (grant nos. 2017M613137 and 2018M643649). The SEM work was done at the International Center for Dielectric Research (ICDR), Xi'an Jiaotong University, Xi'an, China. The work at Northwestern University was supported in part by the LEAP Center, an Energy Frontier Research Center funded by the U.S. Department of Energy, Office of Science, and Office of Basic Energy Sciences under award DE-SC0001059 (sample fabrication and characterization).

AUTHOR CONTRIBUTIONS

Z.W. and C.R. conceived the idea and designed the experiment. L.L., J.X., and J.D. synthesized the PPA and characterized the samples and analyzed the data. C.R. and W.G. fabricated, characterized, and optimized perovskite thin film and PSC devices. J.L. carried out and analyzed the theoretical calculation. W.G., J.X., H.D., B.J., I.S., and C.D.M. provided constructive discussion on the experimental data. Y.Y. and X.G. carried out the 2D-GIXRD and analyzed the data. Z.W. supervised this project.

C.R., M.G.K., and Z.W. wrote the manuscript and all authors contributed to the editing of the manuscript.

DECLARATION OF INTERESTS

The authors declare no competing interests.

Received: March 27, 2019
Revised: July 13, 2019
Accepted: August 28, 2019
Published: October 9, 2019

REFERENCES

1. Brenner, T.M., Egger, D.A., Kronik, L., Hodes, G., and Cahen, D. (2016). Hybrid organic-inorganic perovskites: low-cost semiconductors with intriguing charge-transport properties. Nat. Rev. Mater. *1*, 15007.

2. Di Giacomo, F., Fakharuddin, A., Jose, R., and Brown, T.M. (2016). Progress, challenges and perspectives in flexible perovskite solar cells. Energy Environ. Sci. *9*, 3007–3035.

3. Huang, J., Yuan, Y., Shao, Y., and Yan, Y. (2017). Understanding the physical properties of hybrid perovskites for photovoltaic applications. Nat. Rev. Mater. *2*, 17042.

4. Ran, C., Xu, J., Gao, W., Huang, C., and Dou, S.X. (2018). Defects in metal triiodide perovskite materials towards high-performance solar cells: origin, impact, characterization, and engineering. Chem. Soc. Rev. *47*, 4581–4610.

5. Xi, J., Xi, K., Sadhanala, A., Zhang, K.H.L., Li, G., Dong, H., Lei, T., Yuan, F., Ran, C., Jiao, B., et al. (2019). Chemical sintering reduced grain boundary defects for stable planar perovskite solar cells. Nano Energy *56*, 741–750.

6. Certified best cell efficiency from NREL. https://www.nrel.gov/pv/assets/pdfs/best-research-cell-efficiencies-190416.pdf.

7. Babayigit, A., Ethirajan, A., Muller, M., and Conings, B. (2016). Toxicity of organometal halide perovskite solar cells. Nat. Mater. *15*, 247–251.

8. Shi, Z.J., Guo, J., Chen, Y.H., Li, Q., Pan, Y.F., Zhang, H.J., Xia, Y.D., and Huang, W. (2017). Lead-free organic-inorganic hybrid perovskites for photovoltaic applications: recent advances and perspectives. Adv. Mater. *29*.

9. Ran, C., Wu, Z., Xi, J., Yuan, F., Dong, H., Lei, T., He, X., and Hou, X. (2017). Construction of compact methylammonium bismuth iodide film promoting lead-free inverted planar heterojunction organohalide solar cells with open-circuit voltage over 0.8 V. J. Phys. Chem. Lett. *8*, 394–400.

10. Abate, A. (2017). Perovskite solar cells go lead free. Joule *1*, 659–664.

11. Chen, M., Ju, M.G., Garces, H.F., Carl, A.D., Ono, L.K., Hawash, Z., Zhang, Y., Shen, T., Qi, Y., Grimm, R.L., et al. (2019). Highly stable and efficient all-inorganic lead-free perovskite solar cells with native-oxide passivation. Nat. Commun. *10*, 16.

12. Xu, H., Jiang, Y., He, T., Li, S., Wang, H., Chen, Y., Yuan, M., and Chen, J. (2019). Orientation regulation of tin-based reduced-dimensional perovskites for highly efficient and stable photovoltaics. Adv. Funct. Mater.

13. Jokar, E., Chien, C.H., Tsai, C.M., Fathi, A., and Diau, E.W.G. (2019). Robust tin-based perovskite solar cells with hybrid organic cations to attain efficiency approaching 10%. Adv. Mater. *31*, e1804835.

14. Shao, S., Dong, J., Duim, H., ten Brink, G.H., Blake, G.R., Portale, G., and Loi, M.A. (2019). Enhancing the crystallinity and perfecting the orientation of formamidinium tin iodide for highly efficient Sn-based perovskite solar cells. Nano Energy *60*, 810–816.

15. Chen, K., Wu, P., Yang, W.Q., Su, R., Luo, D.Y., Yang, X.Y., Tu, Y.G., Zhu, R., and Gong, Q.H. (2018). Low-dimensional perovskite interlayer for highly efficient lead-free formamidinium tin iodide perovskite solar cells. Nano Energy *49*, 411–418.

16. Wang, F., Jiang, X., Chen, H., Shang, Y., Liu, H., Wei, J., Zhou, W., He, H., Liu, W., and Ning, Z. (2018). 2D-quasi-2D-3D hierarchy structure for tin perovskite solar cells with enhanced efficiency and stability. Joule *2*, 2732–2743.

17. Shao, S.Y., Liu, J., Portale, G., Fang, H.H., Blake, G.R., ten Brink, G.H., Koster, L.J.A., and Loi, M.A. (2018). Highly reproducible Sn-based hybrid perovskite solar cells with 9% efficiency. Adv. Energy Mater. *8*.

18. Liao, Y.Q., Liu, H.F., Zhou, W.J., Yang, D.W., Shang, Y.Q., Shi, Z.F., Li, B.H., Jiang, X.Y., Zhang, L.J., Quan, L.N., et al. (2017). Highly oriented low-dimensional tin halide perovskites with enhanced stability and photovoltaic performance. J. Am. Chem. Soc. *139*, 6693–6699.

19. Ran, C., Xi, J., Gao, W., Yuan, F., Lei, T., Jiao, B., Hou, X., and Wu, Z. (2018). Bilateral interface engineering toward efficient 2D-3D bulk heterojunction tin halide lead-free perovskite solar cells. ACS Energy Lett. *3*, 713–721.

20. Jokar, E., Chien, C.H., Fathi, A., Rameez, M., Chang, Y.H., and Diau, E.W.G. (2018). Slow surface passivation and crystal relaxation with additives to improve device performance and durability for tin-based perovskite solar cells. Energy Environ. Sci. *11*, 2353–2362.

21. Liu, X., Yan, K., Tan, D., Liang, X., Zhang, H., and Huang, W. (2018). Solvent engineering improves efficiency of lead-free tin-based hybrid perovskite solar cells beyond 9%. ACS Energy Lett. *3*, 2701–2707.

22. Kim, H., Lee, Y.H., Lyu, T., Yoo, J.H., Park, T., and Oh, J.H. (2018). Boosting the performance and stability of quasi-two-dimensional tin-based perovskite solar cells using the formamidinium thiocyanate additive. J. Mater. Chem. A *6*, 18173–18182.

23. Ke, W., Priyanka, P., Vegiraju, S., Stoumpos, C.C., Spanopoulos, I., Soe, C.M.M., Marks, T.J., Chen, M.C., and Kanatzidis, M.G. (2018). Dopant-free tetrakis-triphenylamine hole transporting material for efficient tin-based perovskite solar cells. J. Am. Chem. Soc. *140*, 388–393.

24. Yu, B.B., Xu, L., Liao, M., Wu, Y., Liu, F., He, Z., Ding, J., Chen, W., Tu, B., Lin, Y., et al. (2019). Synergy effect of both 2,2,2-trifluoroethylamine hydrochloride and SnF_2 for highly stable $FASnI_{3-x}Cl_x$ perovskite solar cells. Sol. RRL *3*.

25. Zhao, Z.R., Gu, F.D., Li, Y.L., Sun, W.H., Ye, S.Y., Rao, H.X., Liu, Z.W., Bian, Z.Q., and Huang, C.H. (2017). Mixed-organic-cation tin iodide for lead-free perovskite solar cells with an efficiency of 8.12%. Adv. Sci. *4*, 1700204.

26. Xi, J., Wu, Z., Jiao, B., Dong, H., Ran, C., Piao, C.C., Lei, T., Song, T.B., Ke, W.J., Yokoyama, T., et al. (2017). Multichannel interdiffusion driven $FASnI_3$ film formation using aqueous hybrid salt/polymer solutions toward flexible lead-free perovskite solar cells. Adv. Mater. *29*.

27. Ke, W.J., Stoumpos, C.C., Zhu, M.H., Mao, L.L., Spanopoulos, I., Liu, J., Kontsevoi, O.Y., Chen, M., Sarma, D., Zhang, Y.B., et al. (2017). Enhanced photovoltaic performance and stability with a new type of hollow 3D perovskite (en)$FASnI_3$. Sci. Adv. *3*, e1701293.

28. Liao, W.Q., Zhao, D.W., Yu, Y., Grice, C.R., Wang, C.L., Cimaroli, A.J., Schulz, P., Meng, W.W., Zhu, K., Xiong, R.G., et al. (2016). Lead-free inverted planar formamidinium tin triiodide perovskite solar cells achieving power conversion efficiencies up to 6.22%. Adv. Mater. *28*, 9333–9340.

29. Koh, T.M., Krishnamoorthy, T., Yantara, N., Shi, C., Leong, W.L., Boix, P.P., Grimsdale, A.C., Mhaisalkar, S.G., and Mathews, N. (2015). Formamidinium tin-based perovskite with low E-g for photovoltaic applications. J. Mater. Chem. A *3*, 14996–15000.

30. Lee, S.J., Shin, S.S., Kim, Y.C., Kim, D., Ahn, T.K., Noh, J.H., Seo, J., and Seok, S.I. (2016). Fabrication of efficient formamidinium tin

iodide perovskite solar cells through SnF_2-pyrazine complex. J. Am. Chem. Soc. *138*, 3974–3977.

31. Ke, W.J., Stoumpos, C.C., Logsdon, J.L., Wasielewski, M.R., Yan, Y.F., Fang, G.J., and Kanatzidis, M.G. (2016). TiO_2-ZnS cascade electron transport layer for efficient formamidinium tin iodide perovskite solar cells. J. Am. Chem. Soc. *138*, 14998–15003.

32. Zhu, Z.L., Chueh, C.C., Li, N., Mao, C.Y., and Jen, A.K.Y. (2018). Realizing efficient lead-free formamidinium tin triiodide perovskite solar cells via a sequential deposition route. Adv. Mater. *30*.

33. Gao, W., Ran, C., Li, J., Dong, H., Jiao, B., Zhang, L., Lan, X., Hou, X., and Wu, Z. (2018). Robust stability of efficient lead-free formamidinium tin iodide perovskite solar cells realized by structural regulation. J. Phys. Chem. Lett. *9*, 6999–7006.

34. Lee, S.J., Shin, S.S., Im, J., Ahn, T.K., Noh, J.H., Jeon, N.J., Seok, S.I., and Seo, J. (2018). Reducing carrier density in formamidinium tin perovskites and its beneficial effects on stability and efficiency of perovskite solar cells. ACS Energy Lett. *3*, 46–53.

35. Noel, N.K., Stranks, S.D., Abate, A., Wehrenfennig, C., Guarnera, S., Haghighirad, A.A., Sadhanala, A., Eperon, G.E., Pathak, S.K., Johnston, M.B., et al. (2014). Lead-free organic-inorganic tin halide perovskites for photovoltaic applications. Energ. Environ. Sci. *7*, 3061–3068.

36. Song, T.B., Yokoyama, T., Stoumpos, C.C., Logsdon, J., Cao, D.H., Wasielewski, M.R., Aramaki, S., and Kanatzidis, M.G. (2017). Importance of reducing vapor atmosphere in the fabrication of tin-based perovskite solar cells. J. Am. Chem. Soc. *139*, 836–842.

37. Tai, Q., Guo, X., Tang, G., You, P., Ng, T.W., Shen, D., Cao, J., Liu, C.K., Wang, N., Zhu, Y., et al. (2019). Antioxidant grain passivation for air-stable tin-based perovskite solar cells. Angew. Chem. Int. Ed. Engl. *58*, 806–810.

38. Liu, C., Tu, J., Hu, X., Huang, Z., Meng, X., Yang, J., Duan, X., Tan, L., Li, Z., and Chen, Y. (2019). Enhanced hole transportation for inverted tin-based perovskite solar cells with high performance and stability. Adv. Funct. Mater. *29*.

39. Yokoyama, T., Cao, D.H., Stoumpos, C.C., Song, T.B., Sato, Y., Aramaki, S., and Kanatzidis, M.G. (2016). Overcoming short-circuit in lead-free $CH_3NH_3SnI_3$ perovskite solar cells via kinetically controlled gas-solid reaction film fabrication process. J. Phys. Chem. Lett. *7*, 776–782.

40. Cao, D.H., Stoumpos, C.C., Farha, O.K., Hupp, J.T., and Kanatzidis, M.G. (2015). 2D homologous perovskites as light-absorbing materials for solar cell applications. J. Am. Chem. Soc. *137*, 7843–7850.

41. Saidaminov, M.I., Mohammed, O.F., and Bakr, O.M. (2017). Low-dimensional-networked metal halide perovskites: the next big thing. ACS Energy Lett. *2*, 889–896.

42. Chen, A.Z., Shiu, M., Ma, J.H., Alpert, M.R., Zhang, D.P., Foley, B.J., Smilgies, D.M., Lee, S.H., and Choi, J.J. (2018). Origin of vertical orientation in two-dimensional metal halide perovskites and its effect on photovoltaic performance. Nat. Commun. *9*, 1336.

43. Lin, Y., Bai, Y., Fang, Y.J., Wang, Q., Deng, Y.H., and Huang, J.S. (2017). Suppressed ion migration in low-dimensional perovskites. ACS Energy Lett. *2*, 1571–1572.

44. Dai, J., Xi, J., Li, L., Zhao, J., Shi, Y., Zhang, W., Ran, C., Jiao, B., Hou, X., Duan, X., et al. (2018). Charge transport between coupling colloidal perovskite quantum dots assisted by functional conjugated ligands. Angew. Chem. Int. Ed. Engl. *57*, 5754–5758.

45. Dong, H., Xi, J., Zuo, L., Li, J., Yang, Y., Wang, D., Yu, Y., Ma, L., Ran, C., Gao, W., et al. (2019). Conjugated molecules "bridge": functional ligand toward highly efficient and long-term stable perovskite solar cell. Adv. Funct. Mater. *29*.

46. Gao, W., Ran, C., Xi, J., Jiao, B., Zhang, W., Wu, M., Hou, X., and Wu, Z. (2018). High-quality $Cs_2AgBiBr_6$ double perovskite film for lead-free inverted planar heterojunction solar cells with 2.2 % efficiency. ChemPhysChem *19*, 1696–1700.

47. Yang, M., Zhang, T., Schulz, P., Li, Z., Li, G., Kim, D.H., Guo, N., Berry, J.J., Zhu, K., and Zhao, Y. (2016). Facile fabrication of large-grain $CH_3NH_3PbI_{3-x}Br_x$ films for high-efficiency solar cells via CH_3NH_3Br-selective Ostwald ripening. Nat. Commun. *7*, 12305.

48. Kim, M.K., Jeon, T., Park, H.I., Lee, J.M., Nam, S.A., and Kim, S.O. (2016). Effective control of crystal grain size in $CH_3NH_3PbI_3$ perovskite solar cells with a pseudohalide $Pb(SCN)_2$ additive. CrystEngComm. *18*, 6090–6095.

49. Lee, J.W., Bae, S.H., Hsieh, Y.T., De Marco, N., Wang, M.K., Sun, P.Y., and Yang, Y. (2017). A bifunctional lewis base additive for microscopic homogeneity in perovskite solar cells. Chem *3*, 290–302.

50. Han, Q., Bai, Y., Liu, J., Du, K.Z., Li, T., Ji, D., Zhou, Y., Cao, C., Shin, D., Ding, J., et al. Additive engineering for high-performance room-temperature-processed perovskite absorbers with micron-size grains and microsecond-range carrier lifetimes. Energy Environ. Sci. 10, 2365–2371.

51. Xu, W., Lei, G., Tao, C., Zhang, J., Liu, X., Xu, X., Lai, W.Y., Gao, F., and Huang, W. (2018). Precisely controlling the grain sizes with an ammonium hypophosphite additive for high-performance perovskite solar cells. Adv. Funct. Mater. *28*.

52. Hadadian, M., Correa-Baena, J.P., Goharshadi, E.K., Ummadisingu, A., Seo, J.Y., Luo, J.S., Gholipour, S., Zakeeruddin, S.M., Saliba, M., Abate, A., et al. (2016). Enhancing efficiency of perovskite solar cells via N-doped graphene: crystal modification and surface passivation. Adv. Mater. *28*, 8681–8686.

53. Ran, C., Chen, Y., Gao, W., Wang, M., and Dai, L. (2016). One-dimensional 4 1d[6, 6]-phenyl-C 61-butyric acid methyl ester (PCBM) nanorods as an efficient additive for improving the efficiency and stability of perovskite solar cells. J. Mater. Chem. A, 8566–8572.

54. Han, T.H., Lee, J.W., Choi, C., Tan, S., Lee, C., Zhao, Y., Dai, Z., De Marco, N., Lee, S.J., Bae, S.H., et al. (2019). Perovskite-polymer composite cross-linker approach for highly-stable and efficient perovskite solar cells. Nat. Commun. *10*, 520.

55. Yang, Y.G., Feng, S.L., Li, M., Li, F.C., Zhang, C.C., Han, Y.J., Li, L., Yuan, J.Y., Cao, L., Wang, Z.K., et al. (2018). Enormously improved $CH_3NH_3PbI_3$ film surface for environmentally stable planar perovskite solar cells with PCE exceeding 19.9%. Nano Energy *48*, 10–19.

56. Feng, S.L., Yang, Y.G., Li, M., Wang, J.M., Cheng, Z.D., Li, J.H., Ji, G.W., Yin, G.Z., Song, F., Wang, Z.K., et al. (2016). High-performance perovskite solar cells engineered by an ammonia modified graphene oxide interfacial layer. ACS Appl. Mater. Inter. *8*, 14503–14512.

57. Jacobsson, T.J., Correa-Baena, J.P., Halvani Anaraki, E., Philippe, B., Stranks, S.D., Bouduban, M.E., Tress, W., Schenk, K., Teuscher, J., Moser, J.E., et al. (2016). Unreacted PbI_2 as a double-edged sword for enhancing the performance of perovskite solar cells. J. Am. Chem. Soc. *138*, 10331–10343.

58. Pitarch-Tena, D., Ngo, T.T., Vallés-Pelarda, M., Pauporté, T., and Mora-Seró, I. (2018). Impedance spectroscopy measurements in perovskite solar cells: device stability and noise reduction. ACS Energy Lett. *3*, 1044–1048.

59. Zarazua, I., Han, G., Boix, P.P., Mhaisalkar, S., Fabregat-Santiago, F., Mora-Seró, I., Bisquert, J., and Garcia-Belmonte, G. (2016). Surface recombination and collection efficiency in perovskite solar cells from impedance analysis. J. Phys. Chem. Lett. *7*, 5105–5113.

60. Li, Z., Klein, T.R., Kim, D.H., Yang, M.J., Berry, J.J., van Hest, M.F.A.M., and Zhu, K. (2018). Scalable fabrication of perovskite solar cells. Nat. Rev. Mater. *3*, 18017.